

Application of a synthetic extended source for interferometry

Sophie Morel,* Matthew Dubin, Joe Shiefman, and James Burge

College of Optical Sciences, The University of Arizona, Tucson, Arizona 85721, USA

*Corresponding author: sophie.morel20@gmail.com

Received 23 June 2014; revised 3 September 2014; accepted 15 October 2014;
posted 22 October 2014 (Doc. ID 211477); published 17 November 2014

This paper presents the design of a synthetic extended source (SES) that reduces coherent noise in interferometric measurements. The SES uses a fully coherent source for data acquisition to preserve high-contrast interferograms. Multiple measurements are made while the point source is translated according to a prescribed trajectory. The average of the measurements has the effect of using a source with a distribution defined by the trajectory. Thus, the optical system uses a coherent point source, but the data combination synthesizes the behavior of an extended source. A parametric model to quantify measurement noise due to diffraction from small particles is developed and used to evaluate SES designs. Experimental results are shown that validate the modeling. An example of a practical working SES implemented in a custom SPSI interferometer is provided. © 2014 Optical Society of America

OCIS codes: (120.3180) Interferometry; (120.5050) Phase measurement.

<http://dx.doi.org/10.1364/AO.53.007903>

1. Introduction

Development of optical surface fabrication tools have led to the manufacturing of more complex optical surfaces that require higher precision. Thus, testing methods specific to these high-quality complex surfaces are needed. Interferometry is a common metrology tool that has long been used to test classic spherical surfaces. It has been adapted to large aspheric surfaces metrology. An example of such an instrument developed by the Large Optics Fabrication and Testing group is a Fizeau type, computer-generated hologram (CGH) based simultaneous phase-shifting interferometer (SPSI) [1]. Modern interferometers are usually illuminated with a highly coherent laser point source. Although it has the advantage of providing high-contrast fringes, such a source is responsible for coherent noise that comes from ghost reflections, surface defects, or dust particles diffraction. The stray light from these artifacts adds coherently with the test

and reference waves, creates spurious fringes on the interferogram, and introduces phase error in the measurement.

Several solutions have been developed to reduce this coherent noise. For example, low-pass filtering the data removes the mid- to high-spatial frequency noise. However, it also removes data from the test surface. Coherent noise can be reduced by decreasing the source coherence. The source temporal coherence can be decreased by using a polychromatic source. However, this solution requires a specific type of interferometer that must match the pathlength for the two beams that interfere. The source spatial coherence can be reduced by using an extended source. A classic way to create an extended source consists in sending the laser beam on a spinning ground-glass diffuser [2,3] such that the speckles from the ground glass change fast enough to be averaged out during single camera exposure. However, the use of the extended source also reduces fringe contrast for interferometers that do not match pathlengths for the two interferometer beams. A ring source approach, like the Ring of Fire developed by Zygo [4,5], maintains the fringe contrast for their particular geometry.

We note that interferometers with a real-time extended source, such as the ring used by Zygo, can achieve reduction of speckle by averaging multiple measurements while the diffuser is moving. However, the general use of this technique is not practical for other types of interferometers.

We present the technique of reducing coherent measurement noise in interferometers with a synthetic extended source (SES). Each measurement is taken with a coherent point source illumination, and the source moves between each frame acquisition. The unit under test (UUT) is in focus on the detector. As the source moves, the phase measurement from the UUT remains stationary, whereas the phase data from any out of focus artifact is moved on the sensor between each measurement. The phase error from coherent noise is reduced after averaging multiple measurements. A point source is used, and indeed the source is considered as extended, but only when the measurements are averaged. The advantage of the SES is that it provides high-contrast data because each measurement is taken with a point source, and it can be easily implemented in most interferometers. Indeed, the SES can be made with no additional optics, or with optical elements whose error would be reduced after averaging.

This paper presents a method to design an SES that reduces fixed coherent noise in interferometric measurements. Previous papers [6,7] explained the virtual extended source concept. This paper addresses the analytical approach for the design of an SES and analytical quantification of its performance for reducing coherent artifacts from surface contamination. This paper provides a method for estimating the phase error from scattering in all spaces in an interferometer. This estimation is used to choose the optimal SES shape and size that can reduce this error. The method consists of two steps. In Section 2, an analytical description of the phase error from dust particle diffraction is provided. Section 3 quantifies the effect of averaging the measurements as a function of the point source motion. Section 4 provides experimental validation of the particle phase error model and the performance of an SES as well as an example of a working SES implemented in an operational Fizeau interferometer.

This paper is a summary of the author master's thesis [8], which provides a more detailed explanation of the SES design method.

2. Phase Error from Dust Particle Diffraction

A simple model for predicting the dust particle phase error was developed using Fraunhofer diffraction by a circular obscuration. The diffracted wave propagates to the interferometer sensor and interferes with the test and reference waves, introducing phase error. The phase error from a single dust particle is then generalized to multiple particles located on any surface of an interferometer. This model can be applied to any type of interferometer. In the following, a Twyman–Green interferometer in the flat test

configuration is used as an example to illustrate the method.

Several models accurately describe the complex field diffracted by dust particles. Mie scattering gives the general description of light scattering by a spherical particle. Scalar wave approximation is used in the Rayleigh–Sommerfeld diffraction theory, which predicts the Huygens–Fresnel principle. Fresnel diffraction approximates the Huygens spherical secondary sources as sources with a parabolic wavefront. Further simplification is reached with Fraunhofer diffraction, which approximates the Huygens secondary sources as plane waves [9]. Our treatment uses some simplifications to provide a meaningful approximation of the effect to develop parametric relationships related to performance of the SES, rather than focus on the details. The following assumptions were made to simplify the calculations.

- The particles are approximated as circular or linear 2D obscurations [10].
- The dust particle and detector are imaged in the same space using geometric optics. In the following, the image of the particle is considered in detector space. The particle image diameter d takes the magnification ratio m into account $d = md_{\text{particle}}$.
- The particle image diameter d , distance z from the image of the detector, and wavelength λ allow the Fraunhofer approximation. In other words:

$$N_f = \frac{d^2}{\lambda z} \ll 1. \quad (1)$$

- Optical surfaces from the interferometer are far enough away from each other, so that the phase errors from particles on two consecutive surfaces are uncorrelated. In particular, lenses are approximated as single surfaces.

- Aberrations are neglected.
- Diffraction from other optical elements is negligible.

- The analysis assumed collimated light. A generalized treatment for focusing light using equivalent propagation is explained in [11]. For the case of spherical converging or diverging illumination, the same diffraction effect as with collimated illumination applies, except that the propagation distance z is replaced by an equivalent propagation distance Z_e , defined as

$$Z_e = \frac{R_1(R_1 - R_2)}{R_2},$$

where R_1 is the radius of curvature of a spherical wavefront at position 1, R_2 is the wavefront radius of curvature after it propagates to position 2. In addition, some scaling effect applies to the transverse dimension of the diffraction pattern, such that

$$\frac{d_1}{a_1} = \frac{d_2}{a_2} \quad \text{and} \quad \frac{a_1}{R_1} = \frac{a_2}{R_2},$$

where d_1 and a_1 are, respectively, the particle image diameter and the beam diameter at position 1; d_2 and a_2 are the particle image diameter and beam diameter at position 2.

In the following, a collimated illumination in detector space is assumed, and the Fraunhofer theory is used for propagation.

A. Phase Error from a Single Dust Particle

The phase error from a dust particle depends on the particle location in the interferometer. At least four cases need to be treated differently. The particles can be located on the test or reference surface (case *a* in Fig. 1), or double pass in one arm of the interferometer (case *b*), or common path in the illumination subsystem (case *c*) or common path in the imaging sub-system (case *d*).

1. Particle on One Mirror Surface

This is the simplest case because only one beam of the interferometer interacts with the dust particle, and it only does so once. Babinet's principle can be used to estimate the complex field at the detector plane when a small region is obscured in the test beam. The complex field results from the coherent sum of three fields: the reference plane wave \vec{E}_R , and the test wave that is altered by the particle presence $\vec{E}_{T,\text{altered}}$. This last component is made of two terms $\vec{E}_{T,\text{altered}} = \vec{E}_T - \vec{E}_P$. \vec{E}_T is the test plane wave that would arrive on the detector if there were no particle. \vec{E}_P corresponds to the diffracted portion of the test beam. It can be estimated by considering the image of the particle in detector space. The complex diffracted amplitude is expressed as

$$E_P(r, z) = \frac{-i\pi d^2}{4\lambda z} \exp(ikz) \times \exp\left(i\frac{\pi r^2}{\lambda z}\right) \text{somb}\left(\frac{rd}{\lambda z}\right), \quad (2)$$

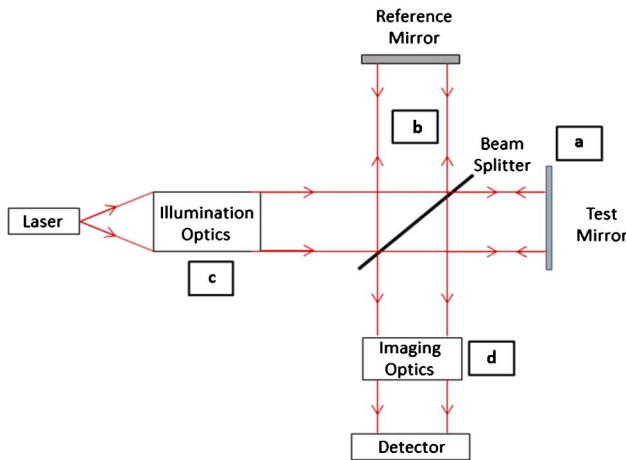


Fig. 1. Twyman-Green interferometer shows four different spaces (a, b, c, and d) where particles can create spurious effects in coherent measurements.

where $k = 2\pi/\lambda$ is the wavenumber, r is the particle image radial coordinates, d is the particle image diameter, and z is the distance between the particle image in detector space and the detector itself. The sombrero function is defined with the Bessel function of the first kind: $\text{somb}(r) = 2J_1(\pi r)/\pi r$.

The total irradiance at the detector is expressed as

$$I(r, z) = \vec{E}(r, z)\vec{E}^*(r, z)\vec{E}(r, z) \\ = \vec{E}_T(r, z) - \vec{E}_P(r, z) + \vec{E}_R(r, z). \quad (3)$$

To simplify the notations, it is assumed that all fields are stationary, have the same orientation, test and reference waves have unit amplitude, and the diffracted pattern is centered at $r = 0$ on the detector plane. Thus,

$$I(r, z) = 2 + 2 \cos(\theta_T - \theta_R) + \left(\frac{\pi d^2}{4\lambda z}\right)^2 \text{somb}^2\left(\frac{rd}{\lambda z}\right) \\ - 2\frac{\pi d^2}{4\lambda z} \text{somb}\left(\frac{rd}{\lambda z}\right) \sin\left(\theta_T - \frac{\pi r^2}{\lambda z}\right) \\ - 2\frac{\pi d^2}{4\lambda z} \text{somb}\left(\frac{rd}{\lambda z}\right) \sin\left(\theta_R - \frac{\pi r^2}{\lambda z}\right), \quad (4)$$

where θ_T and θ_R , respectively, denote the phase error from the test and reference waves.

The phase measurement is obtained after applying a phase-shift algorithm. The four-step phase-shift algorithm was used for its simplicity. For example, if the particle is on the test mirror, and the reference surface is phase-shifted with $\pi/2$ steps, the phase measurement is expressed as

$$\Phi(r, z) = \arctan\left[\frac{I_4(r, z) - I_2(r, z)}{I_1(r, z) - I_3(r, z)}\right] \\ = \arctan\left(\frac{A}{B}\right), \quad \text{with} \\ A = \sin(\theta_T - \theta_R) - \frac{\pi d^2}{4\lambda z} \text{somb}\left(\frac{rd}{\lambda z}\right) \cos\left(\frac{\pi r^2}{\lambda z} - \theta_R\right), \\ B = \cos(\theta_T - \theta_R) - \frac{\pi d^2}{4\lambda z} \text{somb}\left(\frac{rd}{\lambda z}\right) \sin\left(\frac{\pi r^2}{\lambda z} - \theta_R\right). \quad (5)$$

The phase error from the dust particle is deduced from Eq. (5) by assuming that the test and reference waves introduce no error; that is to say when $\theta_T = \theta_R = 0$:

$$\Phi_{\text{particle}}(r, z) = \arctan\left(\frac{A}{B}\right), \quad \text{with} \\ A = -\frac{\pi d^2}{4\lambda z} \text{somb}\left(\frac{rd}{\lambda z}\right) \cos\left(\frac{\pi r^2}{\lambda z}\right) \\ B = 1 - \frac{\pi d^2}{4\lambda z} \text{somb}\left(\frac{rd}{\lambda z}\right) \sin\left(\frac{\pi r^2}{\lambda z}\right). \quad (6)$$

Equation (6) can be simplified under the Fraunhofer approximation. From Eq. (1), the phase

error from a dust particle is equivalent to the argument of the arctangent function, using the small angle approximation:

$$\Phi_{\text{particle}}(r, z) \approx -\frac{\pi d^2}{4\lambda z} \text{somb}\left(\frac{rd}{\lambda z}\right) \cos\left(\frac{\pi r^2}{\lambda z}\right). \quad (7)$$

The phase error would be simply the opposite from Eq. (7) if the particle was on the reference surface. The phase error peak amplitude is proportional to the square of the particle image diameter and inversely proportional to the distance between the image of the particle and the detector plane. The phase error pattern is delimited by a sombrero envelope, whose first zero position is inversely proportional to the particle image diameter and proportional to the observation distance. The phase error is modulated by a cosine function with a square argument.

The case with the particle on the test surface is special when the test surface is imaged onto the detector, so $z = 0$. In this case, the particle on the test mirror causes no measurement error, but may cause a small obscuration in the test.

Figure 2 shows the phase error pattern from a 100 μm diameter particle at equivalent propagation distance of 150 mm.

2. Particle Double-Pass on One Arm of the Interferometer

For example, assume that the dust particle is located at distance $\Delta z/2$ from the test surface and the image of the dust particle is at equivalent propagation distance z from the detector. This is a five beam interference problem. The reference plane wave adds coherently with the altered test wave. That term results from the difference between the ideal plane test wave if the particle was not present and three diffracted fields. One corresponds to the wave that is first diffracted by the particle, then reflects off the test surface, and propagates to the detector. The second term corresponds to the test beam that first

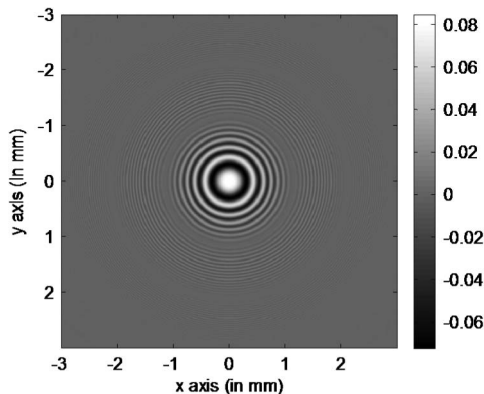


Fig. 2. Phase error from a dust particle located on one mirror surface (in radians). Particle image diameter is $d = 100 \mu\text{m}$ and observation distance is $z = 150 \text{ mm}$.

reflects off the test surface and then is diffracted by the particle. Finally, the last term corresponds to the beam that is first diffracted by the particle on its way to the test mirror, then reflects off the test surface, and is diffracted again by the particle. The amplitude of this double diffracted beam is assumed to be negligible with respect to the other fields.

The same process is repeated to calculate the particle phase error. Under the Fraunhofer approximation, it results in the sum of two phase terms:

$$\begin{aligned} \Phi_{\text{particle}}(r, z) = & -\frac{\pi d^2}{4\lambda z} \text{somb}\left(\frac{rd}{\lambda z}\right) \cos\left(\frac{\pi r^2}{\lambda z}\right) \\ & -\frac{\pi d^2}{4\lambda(z + \Delta z)} \text{somb}\left[\frac{rd}{\lambda(z + \Delta z)}\right] \\ & \times \cos\left[\frac{\pi r^2}{\lambda(z + \Delta z)}\right], \end{aligned} \quad (8)$$

One phase term shows that the diffracted field propagated over a larger distance. The additional defocus depends on the particle location with respect to the test surface.

3. Particle Common-Path in the Illumination Subsystem

Again, the reference beam adds coherently to the test beam. In this configuration, both test and reference waves are altered by the particle presence because the particle diffracts the incident beam before it is divided by the beam splitter. If the test and reference surfaces are ideally flat and path-matched, there is no phase error introduced by the particle. If the two surfaces are not path-matched, there are two images of the dust particle. Referring to our second assumption, the images of the particle and of the detector are considered in the same space. For example, in detector space, we call OPD the equivalent separation distance between the image of the particle through the test surface and the image of the particle through the reference surface.

The phase error from the dust particle results from the difference of two phase terms:

$$\begin{aligned} \Phi_{\text{particle}}(r, z) = & -\frac{\pi d^2}{4\lambda z} \text{somb}\left(\frac{rd}{\lambda z}\right) \cos\left(\frac{\pi r^2}{\lambda z}\right) \\ & + \frac{\pi d^2}{4\lambda(z + \text{OPD})} \text{somb}\left[\frac{rd}{\lambda(z + \text{OPD})}\right] \\ & \times \cos\left[\frac{\pi r^2}{\lambda(z + \text{OPD})}\right]. \end{aligned} \quad (9)$$

Equation (9) was derived for the case where test and reference arms introduce the same magnification ratio, with d being the diameter for both particle images. If the test arm introduces magnification m_T , and the reference arm introduces magnification m_R , the image diameter d would be replaced by $d_T = m_T d$ in the first line of Eq. (9) and by $d_R = m_R d$ in

the second line. One term shows that the diffracted field propagates over a larger distance in one arm than in the other arm because test and reference surfaces are not path-matched.

4. Particle Common-Path in the Imaging Subsystem

The particle is illuminated by the reference and test waves after they have been recombined by the beam splitter. In the ideal case, where test and reference mirrors are perfectly aligned to each other, and there are no aberrations, the particle is perfectly common path. Therefore, its phase error cancels out. In reality, the test and reference waves have some misalignment. It is easy to estimate the error from the dust particle when one of the surfaces is tilted. For example, assume that the reference wave is an ideal plane wave, and the test mirror is tilted with angle α about the y axis. In detector space, the image of the test surface is tilted with angle $2\alpha/m$, where m is the magnification ratio between the test mirror space and the detector space. The particle shadow projected through the reference mirror has a different location on the detector plane than the projected shadow through the test mirror, as shown in Fig. 3. The corresponding shear distance Δx on the detector plane is related to the mirror tilt angle α and the defocus distance z of the particle image from the detector:

$$\Delta x \approx \frac{2\alpha}{m}z.$$

The phase error results from the difference of two terms, with one phase error that is laterally shifted on the detector plane:

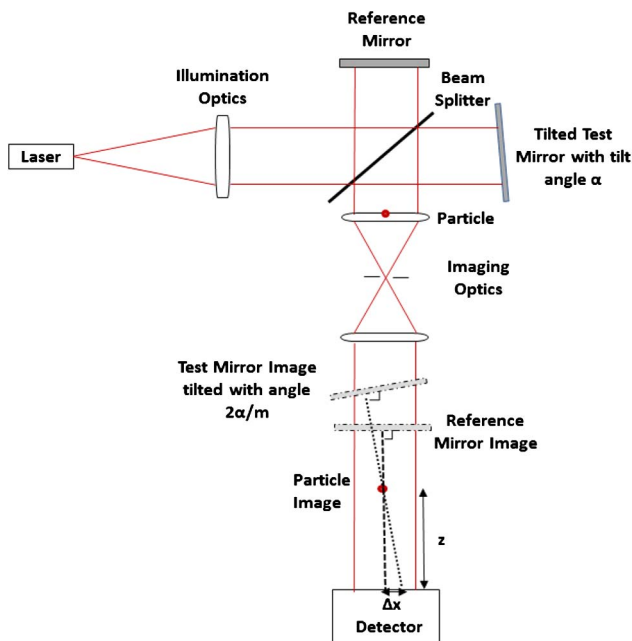


Fig. 3. Particle in the imaging space.

$$\begin{aligned} \Phi_{\text{particle}}(r, z) &= \frac{\pi d^2}{4\lambda z} \text{somb}\left(\frac{rd}{\lambda z}\right) \cos\left(\frac{\pi r^2}{\lambda z}\right) \\ &\quad - \frac{\pi d^2}{4\lambda z} \text{somb}\left(\frac{r_s d}{\lambda z}\right) \cos\left(\frac{\pi r_s^2}{\lambda z}\right) r \\ &= \sqrt{x^2 + y^2} r_s = \sqrt{(x - \Delta x)^2 + y^2}. \end{aligned} \quad (10)$$

Note that this treatment is valid for the case where angle α is created with aberrations as well as misalignment.

B. Multiple Particles Phase Error

The phase error from a single dust particle has been derived for different particle location in an interferometer. In practice, dust particles may be located on all optical surfaces of an instrument. The complex field diffracted by multiple particles that are on the same surface S_j results from the Fourier transform of all the obscuration functions that model the particles. Since the Fourier transform is a linear process, the total diffracted field from surface S_j is simply the coherent sum of each particle i diffracted amplitudes.

$$E_{s_j}(z_j) = \sum_i E(r_i, d_i, z_j). \quad (11)$$

Irradiance and phase are calculated using the same process as before. Under the Fraunhofer and small angle approximations, the phase error is equivalent to the numerator of the arctangent argument [Eq. (7)]. Thus, it is proportional to the Fourier transform of the particle function. Therefore, in the Fraunhofer region, the phase error calculation is a linear process, and the total phase error from multiple dust particles located on the same surface is simply the sum of individual particle phase error:

$$\Phi_{s_j}(z_j) = \sum_i \Phi_i(r_i, d_i, z_j). \quad (12)$$

Equation (4) is used to neglect any interactions between particles that are on different optical surfaces. The same process is repeated for all surfaces. All complex fields interfere with each other, and the phase is derived from the phase-shift algorithm. Again, the phase error is an arctangent function with a rational argument. Its numerator is made of the sum of multiple terms, and each term corresponds to a particle diffraction. Under the Fraunhofer and small angle approximations, the phase error is equivalent to the numerator of the arctangent argument. Therefore, the total phase error results from the sum of each particle's approximated phase error:

$$\Phi_{\text{total}} = \sum_i \Phi_i(r_i, d_i, z_j). \quad (13)$$

Each individual particle phase error Φ_i depends on the particle location in the interferometer, as previously explained.

A model for estimating the phase error from dust particles in an interferometer was developed. This estimation will be used to design the SES.

3. Coherent Noise Reduction with SES

A common way to decrease the phase error is to use an extended source. However, it can reduce the fringe contrast. Another solution consists in using an SES: phase measurements are taken with a coherent point source illumination, providing high-visibility fringes from the test and reference surfaces. An optomechanical system moves the point source between each phase measurement. Using appropriate interferometer geometry, the coherent noise from artifacts or dust particles is reduced after averaging multiple measurements, while the test surface phase data remains stationary [6,7].

It is useful to consider again the image of the source, particle, and detector in the same space in order to predict the particle shadow motion. In the following, everything is imaged in detector space.

The interferometer is illuminated with a laser point source. The wavefront is collimated in detector space. In between, the complex optical system that makes up the interferometer can be modeled with its principal planes, as shown in Fig. 4.

As the point source moves with distance ϵ , the out-of-focus diffraction patterns from the dust move on the detector plane. For this simplified analysis, we treat the image of the dust particle in detector space where the wavefront is collimated. According to [12], the source motion ϵ is directly related to an angular change in angle $\Delta\theta$ in detector space:

$$\Delta\theta = \frac{2NA_{\text{source}}\epsilon}{D}, \quad (14)$$

where NA_{source} is the numerical aperture (NA) of the source, and D is the beam diameter in detector space. The distance between the particle image in detector space and the detector plane is z . Assuming that the source motion is such that the small angle approximation can be used in detector space, the diffraction pattern is shifted by distance s on the detector plane:

$$s = (x_i, y_i) = z(\Delta\theta_x, \Delta\theta_y). \quad (15)$$

Multiple phase measurements are taken for different source positions. The phase error from any out of focus artifact is decreased after averaging all phase

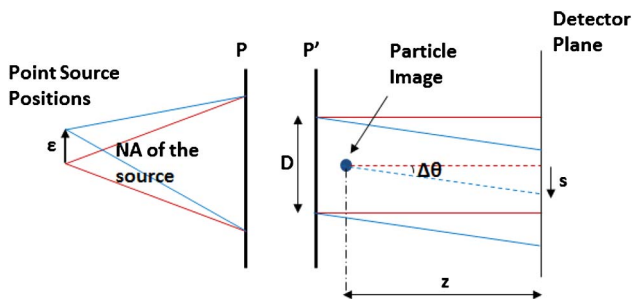


Fig. 4. Effect of the source motion on the particle diffraction pattern.

measurements. The UUT is in focus with the detector. Reference [13] provides an example of an SES interferometer with a system of focusing mirrors as a means to sharply image the UUT on the detector plane. Therefore, the UUT phase measurement remains stationary for any point source position and remains unchanged after averaging all phase maps. This process is called synthetic extended source because the extended source only exists after averaging all data. It is not a physical extended source because each measurement is taken with a point source illumination, which provides high-contrast fringes.

Mathematical analysis is derived to describe the residual phase error from one particle, after applying the SES. Again, the image of the particle is considered in detector space, with image diameter d and distance z between the image and the detector plane. The SES can be described as an array of point sources, modeled with the Dirac delta function. Each Dirac is located at the projection of the point source image through the particle image for each source position. The particle phase error pattern is centered about a Dirac position for each measurement.

The averaged phase is expressed as

$$\begin{aligned} \Phi_{\text{avg}} &= \Phi_{\text{test}} + \Phi_{\text{res}} \Phi_{\text{res}} \\ &= \frac{1}{N} \sum_{i=1}^N \Delta\Phi(x, y) * \delta(x - x_i, y - y_i) \\ &= \frac{1}{N} \Delta\Phi(x, y) * \sum_{i=1}^N \delta(x - x_i, y - y_i), \quad (16) \end{aligned}$$

where Φ_{test} is the UUT phase data, Φ_{res} is the residual phase error from the dust particle after averaging, $\Delta\Phi$ is the particle phase error for one point source illumination, N is the total number of measurements, (x_i, y_i) is the projected location of the source for the i^{th} measurement, and $*$ represents the convolution product. For example, a $N \times M$ grid SES is applied to illustrate this concept. Equation (16) becomes

$$\begin{aligned} \Phi_{\text{res}}(x, y) &= \frac{1}{NM} \frac{1}{\Delta x \Delta y} \Delta\Phi(x, y) \\ &* \left[\text{rect}\left(\frac{x}{l_x}, \frac{y}{l_y}\right) \text{comb}\left(\frac{x}{\Delta x}, \frac{y}{\Delta y}\right) \right], \quad (17) \end{aligned}$$

where Δx and Δy are the spacing between each Dirac in the x and y directions, and l_x and l_y are the dimensions of the grid SES. Figure 5 shows that the residual phase error decreases as the SES dimension increases.

Although a grid SES is a convenient example to simulate the SES effects, most optical systems are rotationally symmetric, and a source with the same geometrical properties is often easier to implement in practice, in terms of vibration control. In the following, the cylinder function is used to describe a disk SES pattern, and Eq. (17) becomes

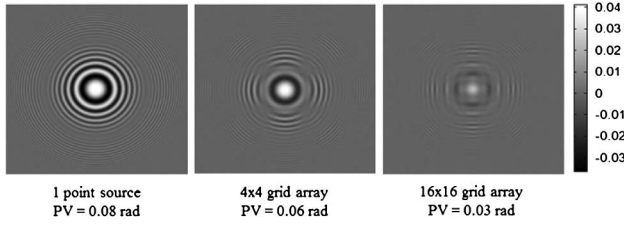


Fig. 5. Residual phase error (in radians) with a grid SES for the case of a dust particle located on one mirror surface. Particle image diameter is $100\ \mu\text{m}$, and observation distance in detector space is $150\ \text{mm}$. (a) Left: phase error from one point source illumination. (b) Middle: from a 4×4 grid of point sources. (c) Right: from a 16×16 grid of point sources.

$$\Phi_{\text{res}}(x,y) = \frac{1}{NM} \frac{1}{\Delta x \Delta y} \Delta \Phi(x,y) * \left[\text{cyl} \left(\frac{\sqrt{x^2 + y^2}}{l} \right) \text{comb} \left(\frac{x}{\Delta x}, \frac{y}{\Delta y} \right) \right]. \quad (18)$$

Since the phase errors for each source position add linearly in the averaging process, and the particle phase error shape does not change with position, this is a linear shift invariant process. From Eq. (16), the SES distribution can be thought of as an impulse response function. Thus, it acts as a transfer function in frequency space. Therefore, some insight can be gained by analyzing the effects of the SES on the phase error frequency content:

$$\begin{aligned} & \text{FT}_{2D} \{ \Phi_{\text{res}}(x,y) \} |_{\xi,\eta} \\ &= \frac{\pi l^2}{4NM} \text{FT}_{2D} \{ \Delta \Phi(x,y) \} |_{\xi,\eta} \\ & \times \left[\text{somb} \left(l \sqrt{\xi^2 + \eta^2} \right) * \text{comb}(\xi \Delta x, \eta \Delta y) \right], \quad (19) \end{aligned}$$

with (ξ, η) being the Fourier variables of (x, y) . The residual phase error frequency content is made of two terms. The first term is the Fourier transform of the dust particle phase error. It is multiplied by the transfer function, which is the Fourier transform of the source distribution.

The Fourier transform of the dust particle phase error is evaluated for the case of a particle located on one mirror surface, as it is the simplest phase error analytic formula. The particle phase error frequency content is expressed as

$$\begin{aligned} \text{FT}_{2D} \{ \Delta \Phi(x,y) \} |_{\xi,\eta} &\approx (\lambda z)^3 \text{disk} \left(\frac{\lambda z}{d} \sqrt{\xi^2 + \eta^2} \right) \\ & * \sin[\pi \lambda z (\xi^2 + \eta^2)]. \quad (20) \end{aligned}$$

The frequency content of the particle phase error is proportional to a disk function, in which size is linear with the particle diameter but inversely proportional to the wavelength and observation distance. This disk function is convolved with a sinusoidal function that has a quadratic argument.

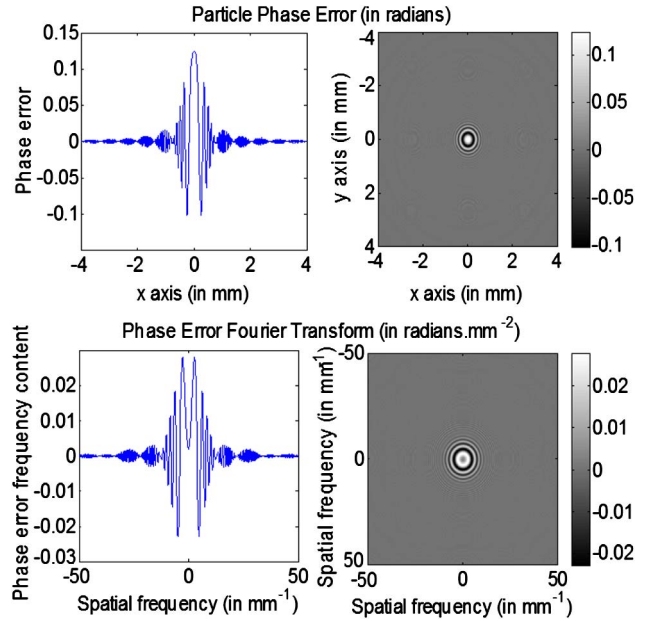


Fig. 6. Phase error (top) and its Fourier transform (bottom) from a $100\ \mu\text{m}$ dust particle at $100\ \text{mm}$ image observation distance.

Figure 6 displays the phase error (top) and the phase error frequency content (bottom) from a dust particle with $100\ \mu\text{m}$ image diameter in detector space, at $z = 100\ \text{mm}$ image distance from the detector.

When the SES is applied, the phase error frequency content is multiplied by the SES transfer function. The last term in Eq. (19) can be simplified by considering that the spacing between each Dirac tends to zero, and the transfer function is simply a sombrero function. Figure 7 shows the effect of the sombrero transfer function on the particle phase error frequency content.

The disk source transfer function attenuates the high spatial frequencies. It does not significantly affect the very low spatial frequencies, but some middle frequencies are cut when the red sombrero curve crosses the zero axis. The negative amplitude

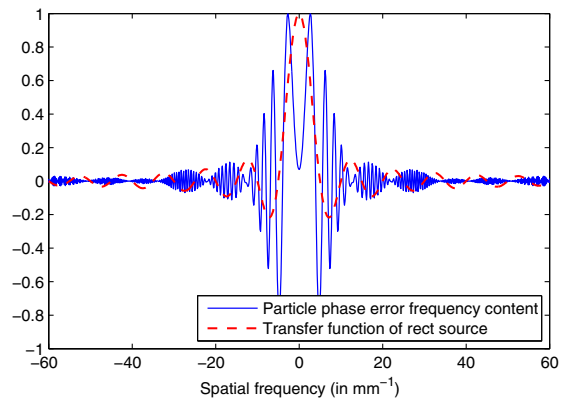


Fig. 7. Normalized particle phase error frequency content and transfer function from a disk SES. Particle image diameter is $d = 100\ \mu\text{m}$ at $z = 100\ \text{mm}$ observation distance in detector space. The disk SES diameter in detector space is $l = 0.2\ \text{mm}$.

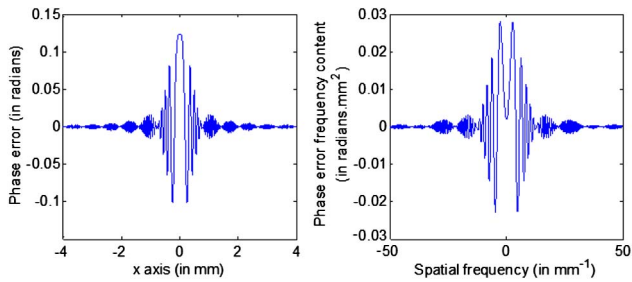


Fig. 8. Particle phase error (left) and its Fourier transform (right). Particle image in detector space is 100 μm diameter and the distance between the particle image and detector is 100 mm.

of the transfer function indicates that a π phase shift applies to the frequency content. This phase shift is not important for this analysis; therefore, the magnitude of the transfer function will be displayed in the following plots. In addition, amplitudes do not need to be exact for this analysis, and normalized plots are displayed for better visualization.

Figures 8–11 show the effects of different shapes of SES. Figure 8 shows the phase error and its frequency content from a 100 μm image diameter particle at 100 mm image distance from the detector. Figure 9 shows the transfer function and the residual phase error from a ring SES. Figure 10 shows the transfer function and residual phase error from a disk SES. Figure 11 shows the transfer function and residual phase error from a ring convolved with a ring SES.

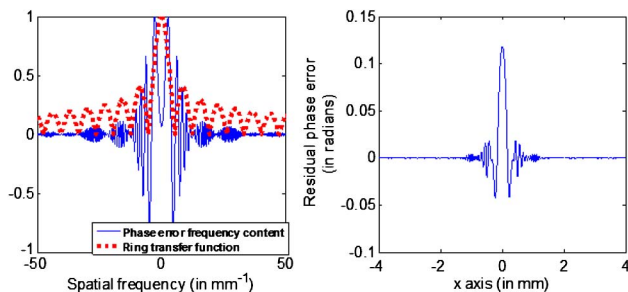


Fig. 9. Normalized phase error frequency content superimposed with the ring SES transfer function (left). Residual phase error (right). The ring SES diameter is $l = 0.1$ mm.

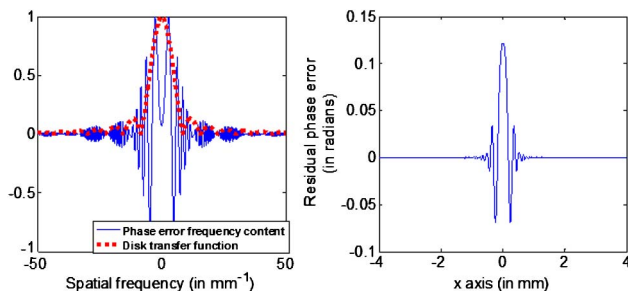


Fig. 10. Normalized phase error frequency content superimposed with the disk SES transfer function (left). Residual phase error (right). The disk SES diameter is $l = 0.1$ mm.

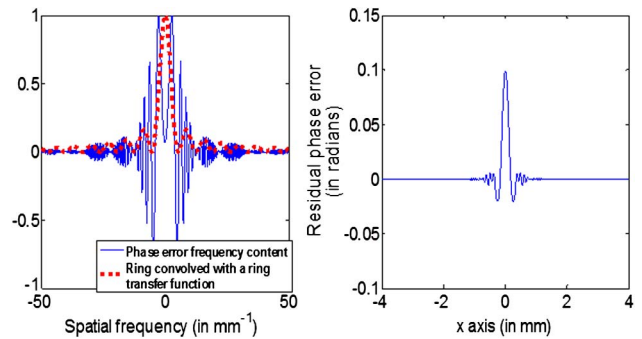


Fig. 11. Normalized phase error frequency content superimposed with the ring convolved with a ring SES transfer function (left). Residual phase error (right). The ring convolved with a ring SES diameter is $l = 0.1$ mm.

The ring SES is probably the simplest solution presented here. However, the ring transfer function has higher-amplitude lobes than the other SES transfer functions. Therefore, it is the least efficient in removing high spatial frequencies. The transfer functions from a disk and from a ring convolved with a ring SES have lower-amplitude lobes and are more efficient in cutting out high spatial frequencies. However, a disk SES is probably more difficult to implement. A ring convolved with a ring is a good solution for efficiently reducing coherent noise, with a simple system, as will be shown in Section 4.C. In addition, the transfer function is narrower for larger SES. Therefore, a large radius SES removes more spatial frequencies.

This analysis was performed for a single particle phase error pattern. Since the phase errors from multiple dust particles add linearly, and because the residual phase error results from a convolution product, which is a linear operation, Eq. (19) generalizes to multiple particles. The total residual phase error is expressed as

$$\text{FT}_{2D}\{\Phi_{\text{res}}(x, y)\}_{|\xi, \eta} = \frac{l_x l_y}{NM} \text{FT}_{2D}\{\Delta\Phi_{\text{tot}}(x, y)\}_{|\xi, \eta} \times [\text{FT}_{2D}\{\text{SES}\}_{|\xi, \eta}] * \text{comb}(\xi\Delta_x, \eta\Delta_y), \quad (21)$$

where $\Delta\Phi_{\text{tot}}$ is the total phase error from all dust particles in the interferometer.

This analysis explained the SES principle and how it can be designed based on the phase error estimation.

4. Experimental Results

An experimental setup was built in order to verify the model of the phase error due to diffraction from a small obscuration and to validate the SES principle.

A. Linear Particle Phase Error

A 125 μm width wire was used to simulate a dust particle in the experimental setup. Such a linear particle

is easier to manipulate than a circular particle. Moreover, the phase pattern from the linear particle is easier to measure because it is modulated by a sinc function that has higher amplitude lobes than the sombrero function. Indeed, the linear particle was modeled with a rect function that is infinite in the y direction. The same process, as with a circular particle, was used to calculate the phase error from a linear particle. For example, the phase error from a linear particle located on one mirror surface is expressed as

$$\Phi_{\text{wire}(x,z)} = \arctan\left(\frac{A}{B}\right), \quad \text{with}$$

$$A = \sin(\theta_T - \theta_R) - \frac{d}{\sqrt{\lambda z}} \text{sinc}\left(\frac{dx}{\lambda z}\right) \cos\left(\frac{\pi x^2}{\lambda z} - \theta_R\right)$$

$$B = \cos(\theta_T - \theta_R) - \frac{d}{\sqrt{\lambda z}} \text{sinc}\left(\frac{dx}{\lambda z}\right) \sin\left(\frac{\pi x^2}{\lambda z} - \theta_R\right). \quad (22)$$

The particle image width d in detector space was measured by bringing the detector to focus with the wire image and counting the number of pixels it covers. The measured image diameter d was 123 μm . The camera was moved away from the wire image to a controlled distance z . The interferometer was illuminated with a 632.8 nm laser point source. The wire was fixed on a kinematic mount that can be moved to any location in the interferometer. Each measurement consists of two steps. First, a measurement is taken with the wire in the setup. Then another measurement is taken after removing the wire. The difference of these two measurements gives the wire phase error with reduced static noise. The kinematic mount allowed putting back the wire in the same position within $\pm 1 \mu\text{m}$. The phase data was post-processed to remove any noise that was not along the wire direction.

Although the wire phase error was predicted by the theoretical model, slight improvement can be gained by fitting some parameters. The phase pattern lateral position was adjusted to compensate for the arbitrary zero position on the detector. The fitting parameters were the phase error from the test and reference surfaces θ_T and θ_R , and the defocus distance z . An example of nominal and fitted values for the case where the linear particle is on one mirror surface is shown in Table 1.

Experimental results are shown in Fig. 12.

Table 1. Nominal and Fitted Parameters

Parameters	Nominal	Fitted
Distance z (mm)	150	151.7
Phase error from test mirror		
θ_T (radians)	0	0.81
Phase error from reference mirror		
θ_R (radians)	0	-0.61

For the case where the wire is in the imaging optics, the phase error was not fitted. The measurement was taken with aligned mirrors, and if there were no aberrations, the phase error would have been zero. However, the plot axis shows that the phase error is negligible when the particle is located in the imaging subsystem, compared with the other cases.

The phase error spatial frequency is predicted by the analytical model. Some mismatch appears at the edges of the pattern, especially when the particle is a double-pass in one arm. In that case, the particle is not common path and the measurement is more sensitive to vibrations.

The amplitude mismatch could be explained with the presence of aberrations in the system that were not taken into account in the theoretical model. The impact of aberrations was evaluated by simulating the Twyman–Green interferometer in Zemax. This allowed us to easily estimate the system point spread function (PSF). The wire image in detector space is affected by the system aberrations and results from the convolution product between the system PSF and the ideal wire modeled with a rect function (Fig. 13).

The result of this convolution product is normalized and put into the Fraunhofer integral to calculate the diffracted phase error, modified by the system aberrations. The measured and fitted results are displayed in Fig. 14 for the case of a dust particle located in the illumination optics.

Although including the aberrated wire image as the input field in the Fraunhofer calculation better fits the experimental results, the model still overestimates the measured phase. This simulation only took into account the on-axis PSF and did not include field aberrations, which could explain the remaining amplitude mismatch at the edges of the phase error pattern.

However, even if the amplitude prediction does not perfectly match the experimental phase data, the spatial frequencies are predicted by our model. In addition, the model tends to overestimate the actual phase error. Since the purpose of this research is to design an SES that reduces the predicted phase error, it should be acceptable to have a model that moderately overestimates the phase error for most systems. As a result, more actual phase error than what is predicted would be removed.

B. SES Validation

Simple SESs were created to verify the SES principle. First, a two-point SES was simulated by taking phase measurements with the laser point source at two different locations separated 200 μm apart. In collimated detector space, it corresponds to a change in angle of 0.8 mrad and results in the phase error pattern shifting by 120 μm on the detector. A 200 μm line source was simulated by moving the laser point source 10 μm steps between each measurement, which corresponds to the particle phase error pattern shifting over 120 μm on the detector plane.

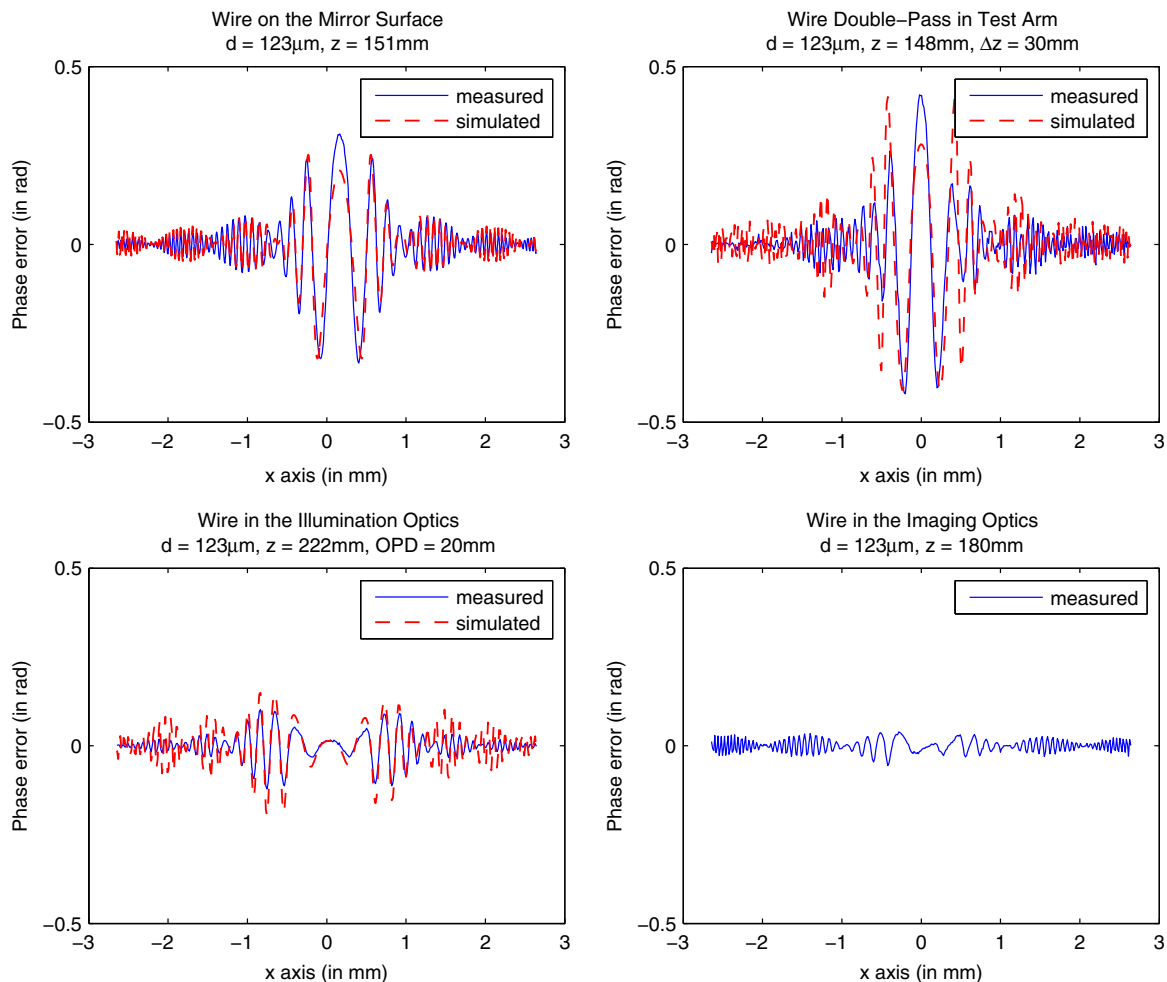


Fig. 12. Measured and simulated (fitted) phase error for different particle locations.

The transfer function from a two-point SES is a cosine function. Therefore, the residual phase error frequency content has periodic zero crossings. Since the spatial frequencies are spatially distributed in the phase error pattern, periodic zero crossings from the cosine transfer function are visible on the residual phase error (Fig. 15).

The transfer function from a line source is a sinc function that attenuates the high spatial frequencies

from the particle phase error frequency content. Since the high-order lobes in the particle phase error contain the high spatial frequency undulations, the sinc transfer function attenuates these side lobes in the residual phase error pattern (Fig. 16).

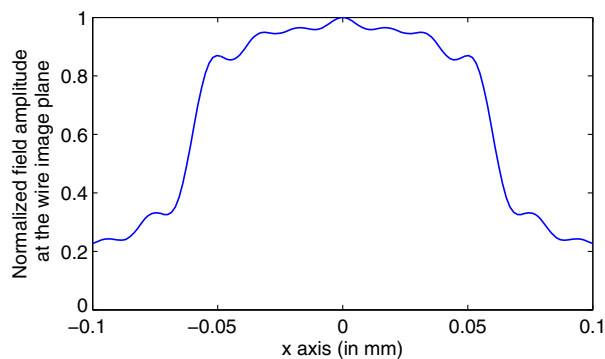


Fig. 13. Normalized field magnitude at the wire image plane, resulting from the convolution of the ideal wire (modeled with a rect function) with the system PSF.

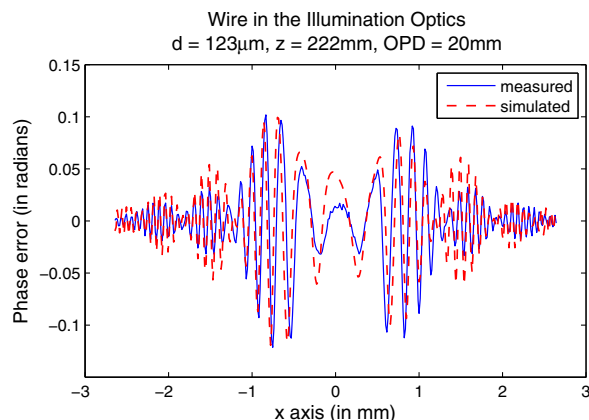


Fig. 14. Measured and simulated (fitted) phase error that takes the system aberrations into account, for the case of a dust particle located in the illumination optics. The phase error amplitude better fits at the edges of the phase error pattern.

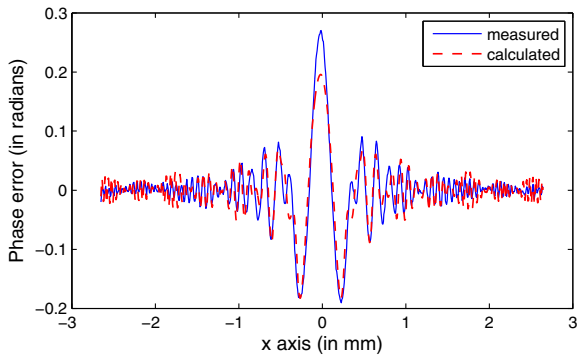


Fig. 15. Residual phase error from a two-point SES.

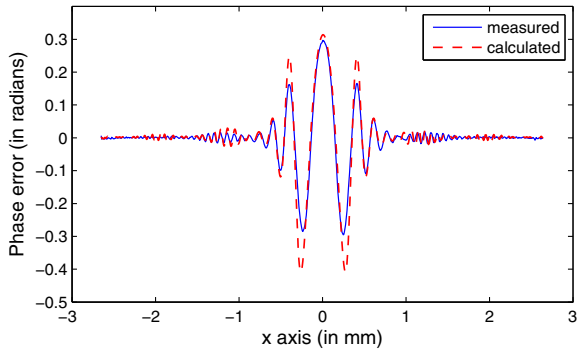


Fig. 16. Residual phase error from a line SES.

These experimental results validate the SES theory and show that the SES can reduce phase error from dust particles.

C. Practical Implementation

This section shows an example of practical implementation of an SES. Many solutions can be used to add tilt to the beam, or move the point source, to create an SES. For example, the laser point source



Fig. 17. SES made of two tilted spinning windows.

could be put on linear stages. However, a spinning system that rotates about the center of gravity of the optics introduces little vibration.

We present an example of a ring convolved with a ring SES that was implemented in a CGH Fizeau polarization-based SPSI interferometer. Because simultaneous phase-shifted frames are measured, the acquisition time is very short, and the source can have continuous motion. The laser point source is divided into two orthogonally polarized point sources that are sent to two spinning windows, as shown in Fig. 17. Since the SES is created after the polarization splitting optics, these elements do not need to be very high quality.

Each window rotates about an axis that is tilted with respect to the window surface normal. Therefore, the window surface is tilted with the beam propagation direction, and the tilt orientation varies as the window is rotating. This causes apparent motion of the source to move in a spiral pattern. The combination of two overlapping spinning tilted windows creates an SES that is a ring convolved with a ring. Figure 18 shows the SES irradiance distribution after averaging the point source motion over multiple window cycles.

Figures 19 and 20 show two phase measurements from a 1 m diameter smooth surface test sphere. Measurements were taken without and with the SES. Figure 21 shows the difference between the two measurements. It displays the coherent noise removed by the SES.

Single point source measurement shows high spatial frequency features that do not appear on the SES measurement. The SES averages out the high spatial frequency noise that comes from speckle, dust particle, or scattering on optical surfaces, revealing the smooth test surface. These experimental data show that a simple SES can be implemented in an interferometer and that it efficiently removes coherent noise.

However, the SES efficiency depends on the averaged number of phase measurements. As the point

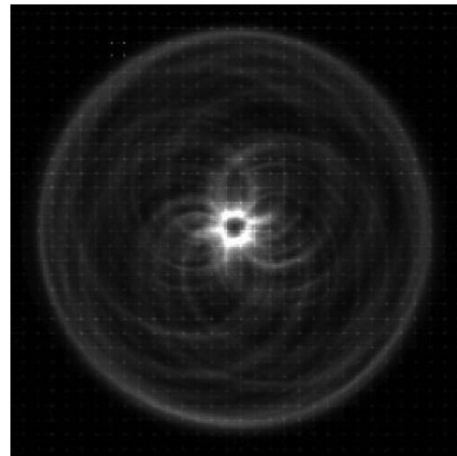


Fig. 18. SES irradiance distribution. The SES is a ring convolved with a ring.

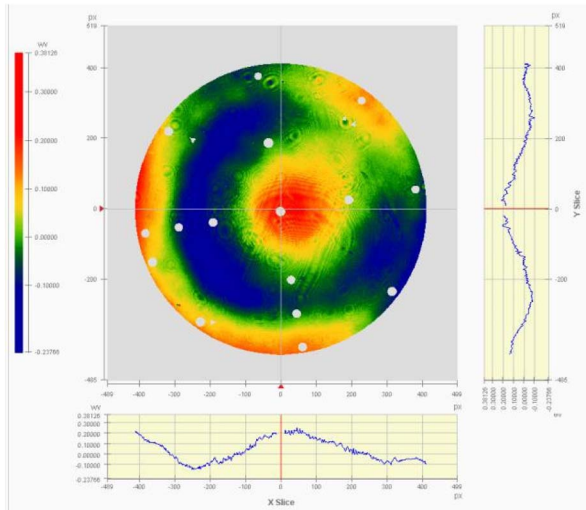


Fig. 19. Fizeau measurement taken with single point source illumination. Peak-to-valley error is $PV = 0.62\lambda$.

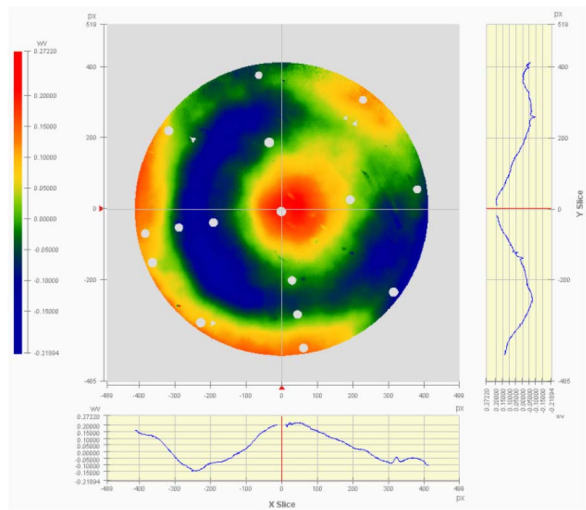


Fig. 20. Fizeau measurement taken with the SES. $PV = 0.49\lambda$.

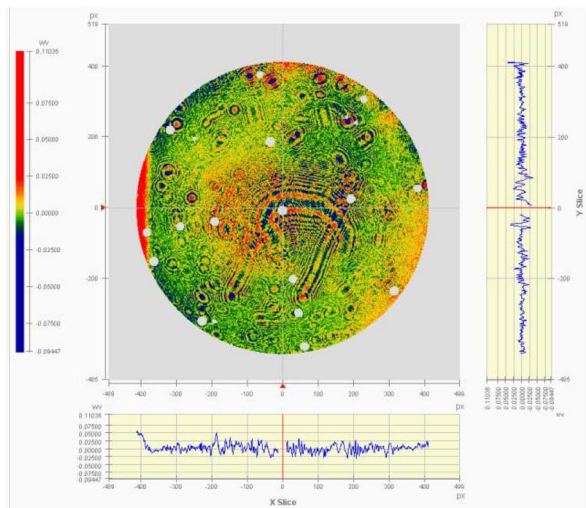


Fig. 21. Fizeau measurement taken with the SES. $PV = 0.20\lambda$.

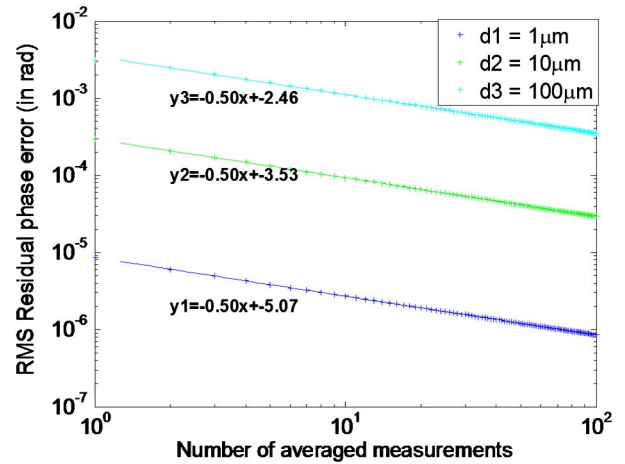


Fig. 22. RMS residual phase error as a function of the number of averaged phase maps for different image particle diameters. Observation distance in detector space is $z = 100$ mm. The cross marks show the simulated residual phase error. The continuous lines correspond to the $1/\sqrt{N}$ fits.

source moves between each measurement, it only results in the shift of the diffraction phase pattern. Therefore, the phase measurements can be considered as uncorrelated, as long as the source motion makes the phase error pattern shift with a distance that is larger than the diffraction pattern itself. In that case, the residual phase error from the SES process is expected to decrease by following the $1/\sqrt{N}$ law, N being the number of phase measurements.

Simulation was performed to illustrate this discussion with a ring SES and a dust particle located on one mirror surface. The particle image diameter in detector space is $100 \mu\text{m}$, and the distance between the particle image and detector plane is 100 mm. The ring SES is such that the particle diffraction pattern is shifted about a circle that is 1 mm diameter on the detector plane. Figure 22 shows the residual phase error for an increasing number of phase measurements in log scale for different particle image diameters.

Measurements are fitted to the log plot of the $1/\sqrt{x}$ function, and the fit equation is displayed on the plot. As expected, phase measurements are uncorrelated, and the residual phase error decreases with the number of averaged measurements, according to the $1/\sqrt{N}$ law.

5. Conclusion

We proposed a method for designing an SES based on coherent noise estimation. The SES maintains high visibility fringes because each measurement is taken with a point source illumination. Multiple measurements are taken for different point source positions. The SES reduces coherent noise after all phase measurements are averaged, while the phase data from the UUT remains stationary. In order to evaluate the SES performance, a model for estimating the phase error from dust particles located in all spaces of an

interferometer was developed. The phase error prediction can be applied to design the SES shape and size. It is used to quantify the SES performance for reducing coherent artifacts from surface contamination. Experimental results validated the phase error estimation model and the SES performance. Qualitative data showed that the SES can be easily implemented in a SPSI interferometer and does remove coherent noise.

References

1. J. H. Burge, C. Zhao, and M. Dubin, "Measurement of aspheric mirror segments using Fizeau interferometry with CGH correction," *Proc. SPIE* **7739**, 773902 (2010).
2. J. Schwider, "Partially coherent illumination in interferometry for optical testing," *Proc. SPIE* **3745**, 2–13 (1999).
3. T. Asakura, "Spatial coherence of laser light passed through rotating ground glass," *Opto-electronics* **2**, 115–123 (1970).
4. M. Kuchel, "Spatial coherence in interferometry. Zygos new method to reduce intrinsic noise in interferometers," *Tech. Rep.* (2004).
5. M. Kuechel, "Apparatus and method(s) for reducing the effects of coherent artifacts in an interferometer," US patent 6,804,011 B2 (12 October 2004).
6. K. R. Freischlad and M. F. Kuechel, "Speckle reduction by virtual spatial coherence," *Proc. SPIE* **1755**, 38–43 (1993).
7. Y. Xu, Y. Wan, and Y. Wu, "Experimental study on virtual spatially extended source," *Proc. SPIE* **8417**, 84173X (2012).
8. S. Morel, "Dust particle phase error in interferometric measurement. Application to the design of synthetic extended source," Master's thesis (College of Optical Sciences, The University of Arizona, 2013).
9. J. W. Goodman, *Introduction to Fourier Optics*, 3rd ed. (Roberts & Company, 2005).
10. J. C. Martinez-Anton, I. Serroukh, and E. Bernabeu, "On Babinet's principle and a diffraction-interferometric technique to determine the diameter of cylindrical wires," *Metrologia* **38**, 125–134 (2001).
11. P. Zhou and J. H. Burge, "Analysis of wavefront propagation using the Talbot effect," *Appl. Opt.* **49**, 5351–5359 (2010).
12. J. H. Burge, "An easy way to relate optical element motion to system pointing stability," *Proc. SPIE* **6288**, 62880I (2006).
13. M. Kuchel, K. H. Schuster, and K. Freischlad, "Method for evaluating interferograms and interferometer therefor," US patent 5,357,341 (18 October 1994).